Humidity Sensing and Photodetection Based on Tin Disulfide Nanosheets

Der-Yuh Lin [1],*, Hung-Pin Hsu [2], Han-Sheng Hu [1], Yu-Cheng Yang [1], Chia-Feng Lin [3] and Wei Zhou [4],*

[1] Department of Electronic Engineering, National Changhua University of Education, No. 2, Shi-Da Road, Changhua 50074, Taiwan; handsome986753@gmail.com (H.-S.H.); M0853002@cc.ncue.edu.tw (Y.-C.Y.)
[2] Department of Electronic Engineering, Ming Chi University of Technology, Taishan, No. 84 Gungjuan Road, New Taipei City 24301, Taiwan; hphsu@mail.mcut.edu.tw
[3] Department of Materials Science and Engineering, National Chung Hsing University, Taichung 402, Taiwan; cflin@dragon.nchu.edu.tw
[4] Key Laboratory of Optoelectronic Devices and Systems of Ministry of Education and Guangdong Province, College of Physics and Optoelectronic Engineering, Shenzhen University, Shenzhen 518060, China
* Correspondence: dylin@cc.ncue.edu.tw (D.-Y.L.); weizhouosu@yahoo.com (W.Z.)

Abstract: Tin disulfide has substantial importance for two-dimensional material-based optoelectronics and sensors due to its unique optoelectrical properties. In this report, we fabricate SnS_2 nanosheets using the low-pressure thermal sulfurization process, whose crystal structure and surface morphology are confirmed by X-ray diffraction (XRD) and scanning electron microscope (SEM) measurements. From photoconductivity measurement and photocurrent mapping, we observe smaller electrode spacing of SnS_2 thin films can enhance photodetection. Then, by the H_2O_2 oxidation processing, we transform SnS_2 to SnO_2 to detect humidity. The measured response and recovery time can be optimized to 5.6 and 1.0 s, respectively, shorter than those of commercial DHT11 humidity sensor of 32 and 34 s. At suitable bias, humidity sensor can detect human respiration properly at room temperature. Our results show that SnS_2 nanosheets exhibit reasonable performance for emergent photodetector applications and humidity sensing.

Keywords: SnS_2; humidity sensor; photoconductivity; respiration rate monitor

1. Introduction

Transition metal dichalcogenides (TMDC) materials [1–3] are attracting intense research interest due to their appreciable band gap in optical and electronical areas. Numerous two-dimensional (2D) hexagonal structures have been widely explored for various applications including photocatalysis [4], supercapacitors [5], optoelectronics [6,7] and sensors [8–10]. TMDCs including MoS_2 [11–13], WS_2 [14], WSe_2 [12,15] and $MoTe_2$ [16] are MX_2 stoichiometric compounds, consisting of periodically stacked one transition metal layer and two chalcogenide layers. Among these TMDC semiconductors—although SnS_2 is less explored compared with MoS_2 or WS_2—tin (Sn) and sulfur (S) are cheap and abundant on the earth and their potential applications have increased fast. Tin disulfide (SnS_2) is an intrinsic n-type layered semiconductor [14] with a band gap of 2.18–2.44 eV [17,18], and it has a layered hexagonal CdI_2 structure with stacked layers with weak van der Waals interaction [19]. Unique characteristics of SnS_2 including high on–off ratios, fast photoresponse rate and good stability [20–22] makes it a promising candidate for a variety of applications in emergent optical and electronic areas. Humidity sensors are very important in modern monitoring field including environmental monitoring, agricultural production, industrial production, biological, medical and chemical monitoring [23,24]. Humidity sensors based on semiconducting oxides have advantages such as low cost, small size and ease of placing in the operating environment. As one important member of metal oxide semiconductors (SnO_2, ZnO, WO_3), tin dioxide is a typical n-type wide semiconductor with

bandgap around 3.7 eV at 300 K [25–27], it has been widely used in various applications such as gas sensors [27,28], solar cells [29] and humidity sensors [30].

In the present work, we synthesized large area SnS_2 films by low pressure sulfurized method. We study the crystal structure and surface morphology of SnS_2 and SnO_2 films by using XRD and SEM measurements, and reveal their optical properties by using the photoconductivity measurement and photocurrent mapping spectroscopy. Optoelectronic response of SnS_2 devices is investigated including response time, responsivity and electrode spacing. Furthermore, the SnO_2 humidity sensor is fabricated by oxidizing SnS_2 film with hydrogen peroxide (H_2O_2). Our work suggests that SnS_2 film has good performance as optical sensors, and SnO_2 is promising humidity sensing material for practical and commercial applications.

2. Materials and Methods

We grow SnS_2 films by low pressure thermal sulfurized method for this study. First, we use E-gun system to evaporate 5/50 nm Ti/Au metallic electrodes on slide glass substrates in a three-zone horizontal tube furnace. Then, we synthesize large area SnS_2 films on metallic electrodes as follows. The source materials in a quartz crucible are 1.2 g sulfur powder and 0.4 g SnO_2 powder, which are placed in the upstream and center of the tube furnace, respectively. Glass substrates are placed 11 cm upstream from the front end of the tube furnace. The center of the tube furnace is kept at 700 °C for 1 h. During the growth process, the carrier gas (Ar gas) has been constantly supplied in a flow rate of 100 sccm, which has also been maintained until the whole furnace temperature gradually decreases down to room temperature. To fabricate SnO_2 humidity sensors, we use 35% hydrogen peroxide (H_2O_2) at 70 °C for 30 min to oxidize SnS_2 film.

We carry out the XRD and SEM measurements to confirm crystal structures and surface morphologies of SnS_2 and SnO_2 films. Their atomic proportion is also determined by energy dispersive X-ray spectrum (EDS). For photoconductivity and photocurrent measurements, a 130 W tungsten–halogen lamp with a monochromator is used to provide monochromatic light, tunable in a wide spectral range by grating. The AC output signal with a chopper frequency of 9 Hz is recorded by a dual phase lock-in amplifier (SR830) to suppress noise signals. The stable bias voltage is supplied by a source meter (Keithley 2400).

The 2D photocurrent mapping of SnS_2 films with different contact spacing are obtained with 520 nm TTL laser illumination; photocurrent signals are recorded by a pico-ammeter (Keithley 6485) with a bias voltage of 20 V. For humidity measurements, we first use carbon dioxide (CO_2) to create a dry environment, then we measure sample resistance with respect to relative humidity at room temperature using a source meter (Keithley 2400)

3. Results and Discussion

Figure 1a shows the SEM image of SnS_2 film on glass substrates. It can be observed that numerous SnS_2 nanosheets are distributed in densely interlaced configurations on the substrate. The continuous SnS_2 film is composed of flower-like surfaces of nanosheets, which has an advantage for photoresponsivity, similar to SnS_2 nanoflake based field effect transistor and high efficiency photodetector [10]. The atomic composition ratio of Sn:S is about 34.6:66.4 (Sn:S = 1:1.98), which is very close to the ideal ratio of SnS_2 (Sn:S = 1:2). Figure 1b shows SEM image of SnO_2 film, fabricated by oxidizing SnS_2 film with hydrogen peroxide (H_2O_2). We anticipate flower-like surface of SnS_2 and SnO_2 films can enhance light absorption and thus photo-responsivity, as well as humidity sensing characteristics. We also observe that the SnO_2 film remained the similar platelet-shaped nanosheets and from the EDS analysis we found that the atomic composition ratio of Sn:O:S is about 27:70:3. A small amount of sulfur has been observed implies that the SnS_2 may not transform into SnO_2 completely. The atomic composition ratio of Sn:O is a little bit higher than the ideal ratio of 1:2, which implies that some oxygen atoms could not find their lattice positions but interstitial sites.
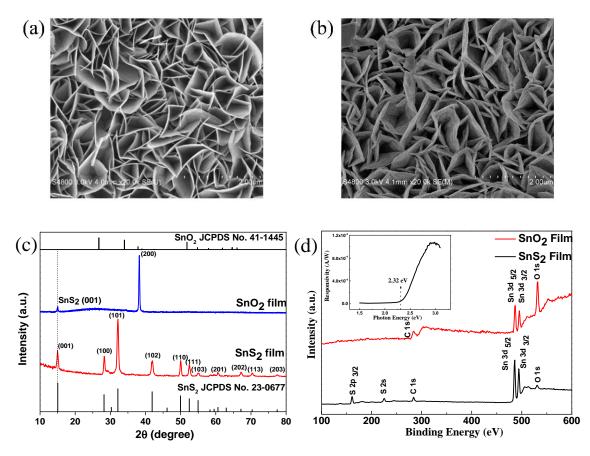
Figure 1. (Color online) (**a**) SEM image of SnS_2 film and (**b**) SnO_2 film oxidized by hydrogen peroxide (H_2O_2); (**c**) X-ray diffraction (XRD) patterns of SnS_2 (red) and SnO_2 (blue) films and SnS_2 and SnO_2 of the JCPDS database (black); (**d**) XPS spectra of SnS_2 (black) and SnO_2 (brown) films. The inset is the photoconductivity measurement of SnS_2 film with band gap of 2.32 eV indicated by the dashed line.

Figure 1c shows XRD patterns for SnS_2 and SnO_2 films. The detected peaks can be attributed to (001), (100), (101), (102), (110), (111), (103), (201), (202), (113) and (203) crystallographic planes of the hexagonal phases SnS_2, as shown for hexagonal SnS_2 (card no. 23-0677) of the JCPDS database. Our results also show good crystal structure of large area SnS_2 films by low pressure thermal sulfurization process. Here, we found that the highest XRD intensity showed (101) preferred orientation, which is similar to the result reported by J. Ma et al. [31] Through anisotropic nucleation at high precursor concentration, three-dimensional aggregation effects may dominate the whole process and develop a flower-like morphology rather than a flat two-dimensional surfaces with a preferred orientation of (001) direction. After oxidization by using H_2O_2, the SnS_2 films have been transformed into SnO_2 films. The sulfide atoms have been substituted by oxygen atoms and rearranged in a new crystal type with a preferred orientation of (200). In the XRD patterns of SnO_2 film, the first weak peak represents the (001) plane of SnS_2 film and the second peak indicates the (200) plane of SnO_2 (card no. 41-1445) of the JCPDS database. The coexistence of SnS_2 and SnO_2 peaks reveals that some residual SnS_2 has not been transformed completely. We think residual SnS_2 nanosheets may coexist with the SnO_2 nanosheets and become a SnO_2/SnS_2 heterojunction structures, which may contribute better response than pure SnO_2 or SnS_2 nanosheets as reported by D. Gu et al. [32]

We are also interested in the obvious (200) peak from SnO_2 film. It may imply the SnO_2 film has been formed in a very disordered phase. The 2θ peak position of the (200) located at 38.24 degree, which is a little bit higher that that indicated in the JCPDS No. 41-1445 (37.88 degree). We think that during the process of oxygen substitution for transformation of SnO_2, some oxygen atoms may insert in possible interstitial positions in the crystals and

extend the lattice a little bit. Actually, the XRD analysis is done with an X-ray source of Cu Kα radiation (λ = 1.5406 Å), and the lattice constant of a is determined to be 4.7 Å for 2θ = 37.88 degree while a = 4.74 Å for 2θ = 38.24 degree. The difference is less than 1%. In Figure 1d, the XPS spectrum of SnS$_2$ film shows a characteristic peak of Sn 3d5/2 and Sn 3d3/2 bands around 486 and 494 eV, respectively. The signals of S 2p and 2s bands are found at the binding energy around 161 and 225 eV, respectively. Furthermore, a weak O 1s peak locates at 531 eV, which may contribute from the native SnO$_2$ layer on the SnS$_2$ surface [33]. The photo-conductivity spectrum in the inset of Figure 1d also illustrates the proper band gap of SnS$_2$ film around 2.32 eV. After oxidization with H$_2$O$_2$, on the SnO$_2$ film, no sulfur related signals have been found and an obvious O 1s band signal has been observed at binding energy of 531 eV consistent with the results of Love et al. [33]. We anticipate H$_2$O$_2$ oxidization can effectively change SnS$_2$ to SnO$_2$, which has good humidity sensing characteristics.

To measure photoresponse and humidity sensing of our devices, we use the home-built AC opto-electronic setup in Figure 2a and humidity measurement system in Figure 4a, respectively. In Figure 2c,d, we show 2D photocurrent mapping of two SnS$_2$ films with electrode spacing of 600 and 800 μm, respectively. The width of the channel is 2000 um and the film thickness is about 5 um. The only difference for the geometrical parameter of the devices is the channel length. In this a pilot study we did not focus on the comparison of different geometrical parameters. The strong photocurrent is generated only in the gap of voltage biased metal-semiconductor-metal fingers. The photocurrent distribution reveals that some area can generate higher current (about two times) than the average value. This fact implies that the uniformity of film quality needs to be improved for applications. The photoinduced carriers may recombine before they can reach the electrodes due to high density of defects in the crystal surface or interfaces. We also notice the electrode spacing has its influence to photodetection, which provides another parameter to optimize device performance.
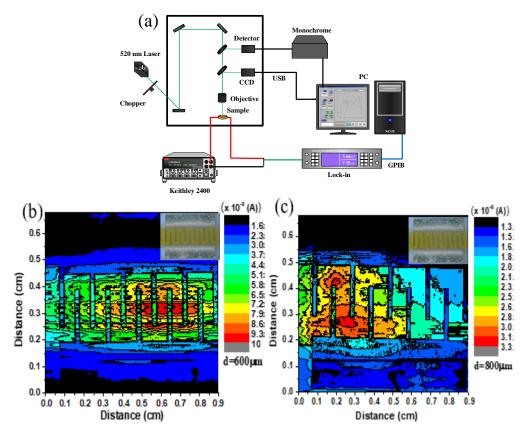

Figure 2. (Color online) (**a**) Scheme of photocurrent measurement: (**b**) and (**c**) 2D photocurrent mapping of SnS$_2$ films with interdigitated electrodes of 600 and 800 μm spacing, respectively. Device optical image is in the upper right corner.

To understand the photoresponse of SnS$_2$ films, including responsivity speed, defect level influence to carrier lifetime and electrode spacing effect, we carry out frequency dependent photoconductivity measurements. In Figure 3a, we present photocurrent results excited by a 405 nm laser at various chopper frequencies. The observed decrease of photocurrent n_{ac} with increasing frequency obeys the relation (1) [34]:

$$n_{ac} = k_1 \times \tan h\left(\frac{1}{4f\tau_1}\right) + k_2 \times \tan h\left(\frac{1}{4f\tau_2}\right) \qquad (1)$$

where n_{ac} is the measured photocurrent, f is the chopper frequency, k_1 and k_2 describe indirect and direct recombination, respectively; τ_1 and τ_2 are carrier lifetime of indirect and direct recombinations. In Table 1, we list fitted k_1, k_2, τ_1 and τ_2 values. When SnS$_2$ film contact spacing changes from 600 to 800 μm, the large variation of k_2 from 0.04 to 0.36 is the main result, indicating defects are decreased due to the shorter spacing electrode. Our results reveal that SnS$_2$ film of 600 μm electrode spacing can have larger photocurrent than that of 800 μm electrode spacing. Figure 3b shows the relative balance [(I$_{max}$ − I$_{min}$)/I$_{max}$] versus frequency up to 10 kHz. The relative balance remains up to 23.4% for the 600 μm electrode spacing SnS$_2$ film at 10 kHz; however, it drops to 9.01% at 30 Hz for the 800 μm electrode spacing SnS$_2$ film and photocurrent becomes too low to be measured at high frequency range. Our observation implies that the SnS$_2$ film with 600 μm contact spacing is capable of monitoring faster optical signals.
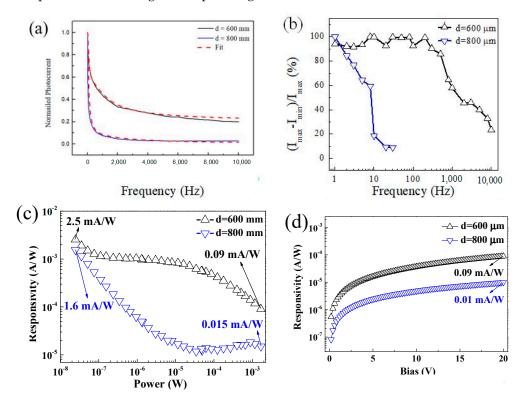

Figure 3. (Color online) (**a**) Frequency response of photoconductivity and time constant fitting of SnS$_2$ film with different finger spacing; (**b**) the relative balance [(I$_{max}$ − I$_{min}$)/Imax] versus frequency of SnS$_2$ film with different finger spacing. (**c**) Laser power and (**d**) bias voltage-dependent photoresponsivity of SnS$_2$ film with different finger spacing.

Table 1. Fitting results of τ_1, τ_2, k_1 and k_2 for SnS$_2$ film with 600 and 800 μm electrode spacing.

Sample	600 μm	800 μm
k_1	0.64	0.96
k_2	0.36	0.04
τ_1 (s)	4.54×10^{-3}	5.26×10^{-3}
τ_2 (s)	2.41×10^{-4}	9.38×10^{-5}

In Figure 3c,d, we compare photoresponsivity of SnS$_2$ films of 600 and 800 μm contact spacing with respect to laser power and bias voltage. At weak 405 nm incident laser intensity of 0.2 μW, the responsivities are 2.55 mA/W and 1.55 mA/W for SnS$_2$ films of 600 and 800 μm contact spacing, respectively. The relative photoresponsivity keeps unchanged with increasing incident laser power. The effect of bias voltage on the photoresponsivity shows the same trend in Figure 3d. For both low and high operating voltages up to 20 V, the responsivity values of the SnS$_2$ film with 600 μm contact spacing is always larger and improves faster than that of the SnS$_2$ film with 800 μm contact spacing. Our results imply shorter contact spacing can improve photoresponsivity for SnS$_2$ film photodetection. Although the underlying mechanism needs further study, we believe the reduced grain boundary of shorter electrode spacing can improve both photodetection as well as the following humidity sensing.

In Figure 4b,c, we show the response and recovery time measurements of SnO$_2$ humidity sensors. For SnO$_2$ sensors of 700 and 900 μm contact spacing and the commercial DHT11 humidity sensor, the measured response times are 5.6, 9.0 and 32 s, and for recovery time 1.0, 1.0 and 34 s, respectively. In general, the sensing mechanism occurring in SnO$_2$ humidity sensors has several hypotheses. Since water is a weak electrolyte, adsorbed water molecules can be dissociated on the surface. On the other hand, free electrons can also be released due to surface interactions between the SnO$_2$ and the adsorbed H$_2$O molecules. [35] H. Y. Xu et al. has reported that the exposed {200} crystal faces have more unsaturated metal bounds and dangling bonds, which resulting in more oxygen vacancies for enhancing the absorption of water molecules. [36]

Our results indicate both SnO$_2$ humidity sensors have faster response than that of the DHT11 sensor. In Figure 4d,e, humidity sensitivity versus relative humidity and bias voltage are measured. Humidity sensitivity has been calculated using the formula:

$$S(\%) = \frac{I_{RH}}{I_{DA}} \tag{2}$$

where I_{RH} and I_{DA} are measured currents at given and initial relative humidity, respectively [37]. Although the trend of resistance decrease with increasing humidity keeps the same for different humidity sensors in Figure 4f, the maximum sensitivity of bias 30 V at room humidity is observed for SnO$_2$ film with 700 μm contact spacing. Our results SnO$_2$ film with 700 μm contact spacing has better response than film of 900 μm contact spacing, same as the situation of SnO$_2$ film photodetection.

Breath monitoring is one important application for fast response humidity sensor. In Figure 4g, the current-time (I-T) plot of the SnO$_2$ film with 700 and 900 μm contact spacing are at bias voltage of 10 V. Each current peak represents one human exhalation, and we also simulate apnea from 60 to 75 s. The observed respiratory rate is 17 breaths per minute, and we can clearly observe the apnea. Even though our samples have not reached their current top at high humidity, they still get the excellent measurement of human exhalation. On the contrary, the DHT11 humidity sensor with longer response time than SnO$_2$ films, cannot apply to human exhalation. The commercial DHT11 has a plastic case to protect the humidity device and which is put in a mask for this test. We think may be the humidity is not very easy to escape out the plastic case and the mask resulting in a constant high humidity curve in Figure 4g. Our experiments show SnS$_2$ film possesses fast response and recovery time to water molecules generated by human exhalation at room temperature.
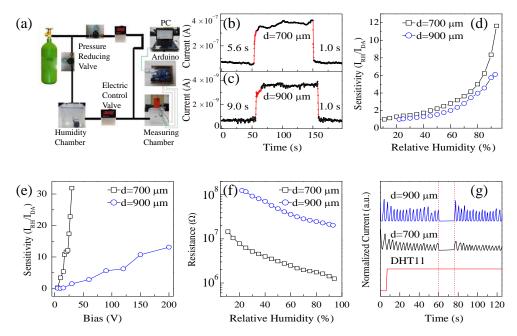
Figure 4. (Color online) (**a**) Scheme of humidity sensing system; (**b**,**c**) humidity response and recovery time of SnO$_2$ film with 700 and 900 μm electrode spacing, respectively; the bias voltage of 10 V has been applied in this test and the two humidity levels used for this test were 15% and 65%, respectively; (**d**) relativity humidity and (**e**) bias voltage-dependent sensitivity of SnO$_2$ film with different finger spacing; (**f**) relativity humidity dependent resistance of SnO$_2$ film with different finger spacing; (**g**) repeatability measurement of three sensor devices upon exposure to human exhalation.

4. Conclusions

In conclusion, we have successfully synthesized high quality SnS$_2$ films by low pressure thermal sulfurization process, confirmed by XRD, Raman and SEM measurements. SnS$_2$ films are composed of nanosheets of flower-like surface and large photoresponsivity up to 2.55 and 1.55 mA/W for electrode spacing of 600 and 800 μm films, and the relative balance can remain as 23.4% for the SnS$_2$ film with 600 μm electrode spacing up to 10 kHz. We further transform SnS$_2$ to SnO$_2$ using H$_2$O$_2$ oxidation process. The humidity sensing analysis showed the SnO$_2$ film has shorter response time than DHT11 humidity sensor, and can be even used to monitor human breathing. Our results indicate short contact spacing not only enhances photoresponsivity significantly but also improves the humidity sensing capability for SnS$_2$ and SnO$_2$ films separately. Our results would provide useful insights into the design, fabrication and practical application of photodetector and humidity sensor based on SnS$_2$ film.

Author Contributions: H.-P.H. and D.-Y.L. conceived and designed the experiments. H.-S.H., Y.-C.Y. and C.-F.L. prepared the materials and performed the experiments. W.Z., D.-Y.L., H.-S.H. and Y.-C.Y. analyzed data. W.Z. and D.-Y.L. wrote the manuscript. All authors have read and agreed to the published version of the manuscript.

Data Availability Statement: Not applicable.

Conflicts of Interest: The authors declare that they have no conflict of interest.

References

1. Tan, H.; Xu, W.; Sheng, Y.; Lau, C.; Fan, Y.; Chen, Q.; Tweedie, M.; Wang, X.; Zhou, Y.; Warner, J. lateral graphene-contacted vertically stacked WS$_2$/MoS$_2$ hybrid photodetectors with large gain. *Adv. Mater.* **2017**, *29*, 1702917. [CrossRef]
2. Fang, H.; Chuang, S.; Chang, T.C.; Takei, K.; Takahashi, T.; Javey, A. High-performance single layered WSe2 p-FETs with chemically doped contacts. *Nano Lett.* **2012**, *12*, 3788–3792. [CrossRef]
3. Li, M.; Shi, Y.; Cheng, C.; Lu, L.; Lin, Y.; Tang, M.; Tsai, M.L.; Chu, C.; Wei, K.; He, J.; et al. Epitaxial growth of a monolayer WSe$_2$-MoS$_2$ lateral p-n junction with an atomically sharp interface. *Science* **2015**, *349*, 524–528. [CrossRef]
4. Zhang, N.; Zhang, Y.; Xu, Y. Recent progress on graphene-based photocatalysts: Current status and future perspectives. *Nanoscale* **2012**, *4*, 5792–5813. [CrossRef]
5. El-Kady, M.; Kaner, R. Scalable fabrication of high-power graphene micro-supercapacitors for flexible and on-chip energy storage. *Nat. Commun.* **2013**, *4*, 1475. [CrossRef] [PubMed]
6. Wang, Q.H.; Kalantar-Zadeh, K.; Kis, A.; Coleman, J.N.; Strano, M.S. Electronics and optoelectronics of two-dimensional transition metal dichalcogenides. *Nat. Nanotechnol.* **2012**, *7*, 699. [CrossRef] [PubMed]
7. Jariwala, D.; Sangwan, V.K.; Lauhon, L.; Marks, T.J.; Hersam, M.C. Emerging device applications for semiconducting two-dimensional transition metal dichalcogenides. *ACS Nano* **2014**, *8*, 1102–1120. [CrossRef] [PubMed]
8. Choi, W.; Choudhary, N.; Han, G.H.; Park, J.; Akinwande, D.; Lee, Y.H. Recent development of two-dimensional transition metal dichalcogenides and their applications. *Mater. Today* **2017**, *20*, 116–130. [CrossRef]
9. Ou, J.Z.; Carey, B.; Ge, W.; Daeneke, T.; Rotbart, A.; Shan, W.; Wang, Y.; Fu, Z.; Chrimes, A.F.; Wlodarski, W. Physisorp-tion-based charge transfer in two-dimensional SnS$_2$ for selective and reversible NO$_2$ gas sensing. *ACS Nano* **2015**, *9*, 10313–10323. [CrossRef]
10. Jia, X.; Tang, C.; Pan, R.; Long, Y.-Z.; Gu, C.; Li, J. Thickness-dependently enhanced photodetection performance of vertically grown SnS$_2$ nanoflakes with large size and high production. *ACS Appl. Mater. Interfaces* **2018**, *10*, 18073–18081. [CrossRef]
11. Svatek, S.A.; Antolin, E.; Lin, D.-Y.; Frisenda, R.; Reuter, C.; Molina-Mendoza, A.J.; Muñoz, M.; Agrait, N.; Ko, T.-S.; de Lara, D.P.; et al. Gate tunable photovoltaic effect in MoS$_2$ vertical p–n homostructures. *J. Mater. Chem. C* **2016**, *5*, 854–861. [CrossRef]
12. Li, H.; Wu, J.; Yin, Z.; Zhang, H. Preparation and applications of mechanically exfoliated single-layer and multilayer MoS$_2$ and WSe$_2$ nanosheets. *Acc. Chem. Res.* **2014**, *47*, 1067–1075. [CrossRef]
13. Radisavljevic, B.; Radenovic, A.; Brivio, J.; Giacometti, V.; Kis, A. Single-layer MoS$_2$ transistors. *Nat. Nanotechnol.* **2011**, *6*, 147–150. [CrossRef]
14. Perea-Lopez, N.; Elías, A.L.; Berkdemir, A.; Castro-Beltran, A.; Gutiérrez, H.R.; Feng, S.; Lv, R.; Hayashi, T.; López-Urías, F.; Ghosh, S.; et al. Photosensor device based on few-layered WS$_2$ Films. *Adv. Funct. Mater.* **2013**, *23*, 5511–5517. [CrossRef]
15. Huang, J.-K.; Pu, J.; Hsu, C.-L.; Chiu, M.-H.; Juang, Z.-Y.; Chang, Y.-H.; Chang, W.-H.; Iwasa, Y.; Takenobu, T.; Li, L.-J. Large-area synthesis of highly crystalline WSe$_2$ Monolayers and device applications. *ACS Nano* **2014**, *8*, 923–930. [CrossRef] [PubMed]
16. Sung, J.H.; Heo, H.; Si, S.; Kim, Y.H.; Noh, H.R.; Song, K.; Kim, J.; Lee, C.-S.; Seo, S.-Y.; Kim, D.-H.; et al. Coplanar semiconductor–metal circuitry defined on few-layer MoTe$_2$ via polymorphic heteroepitaxy. *Nat. Nanotechnol.* **2017**, *12*, 1064–1070. [CrossRef] [PubMed]
17. Burton, L.A.; Whittles, T.; Hesp, D.; Linhart, W.; Skelton, J.M.; Hou, B.; Webster, R.F.; O'Dowd, G.; Reece, C.; Cherns, D.; et al. Electronic and optical properties of single crystal SnS$_2$: An earth-abundant disulfide photocatalyst. *J. Mater. Chem. A* **2015**, *4*, 1312–1318. [CrossRef]
18. Huang, Y.; Sutter, E.; Sadowski, J.; Cotlet, M.; Monti, O.L.; Racke, D.A.; Neupane, M.R.; Wickramaratne, D.; Lake, R.; Parkin-son, B.A.; et al. Tin disulfide—An emerging layered metal dichalcogenide semiconductor: Materials properties and device characteristics. *ACS Nano* **2014**, *8*, 10743–10755. [CrossRef]
19. Ham, G.; Shin, S.; Choi, H.; Park, J.; Lee, J.; Jeon, H. Engineering the crystallinity of tin disulfide deposited at low temperatures. *RSC Adv.* **2016**, *6*, 54069–54075. [CrossRef]
20. Chang, R.-J.; Tan, H.; Wang, X.; Porter, B.; Chen, T.; Sheng, Y.; Zhou, Y.; Huang, H.; Bhaskaran, H.; Warner, J.H. High-performance all 2D-layered tin disulfide: Graphene photodetecting transistors with thickness-controlled interface dynamics. *ACS Appl. Mater. Interfaces* **2018**, *10*, 13002–13010. [CrossRef] [PubMed]
21. Su, G.; Hadjiev, V.; Loya, P.E.; Zhang, J.; Lei, S.; Maharjan, S.; Dong, P.; Ajayan, P.M.; Lou, J.; Peng, H. Chemical vapor deposition of thin crystals of layered semiconductor SnS$_2$ for fast photodetection application. *Nano Lett.* **2015**, *15*, 506–513. [CrossRef]
22. De, D.; Manongdo, J.; See, S.; Zhang, V.; Guloy, A.; Peng, H. High on/off ratio field effect transistors based on exfoliated crystalline SnS$_2$ nano-membranes. *Nanotechnology* **2012**, *24*, 025202. [CrossRef]
23. Song, X.; Qi, Q.; Zhang, T.; Wang, C. A humidity sensor based on KCl-doped SnO$_2$ nanofibers. *Sens. Actuators B Chem.* **2009**, *138*, 368–373. [CrossRef]
24. Bharatula, L.D.; Erande, M.B.; Mulla, I.S.; Rout, C.S.; Late, D.J. SnS$_2$ nanoflakes for efficient humidity and alcohol sensing at room temperature. *RSC Adv.* **2016**, *6*, 105421–105427. [CrossRef]
25. Wang, L.; Wang, S.; Wang, Y.; Zhang, H.; Kang, Y.; Huang, W. Synthesis of hierarchical SnO$_2$ nanostructures assembled with nanosheets and their improved gas sensing properties. *Sens. Actuators B Chem.* **2013**, *188*, 85–93. [CrossRef]
26. Zhang, D.-F.; Sun, L.-D.; Yin, J.-L.; Yan, C.-H. Low-temperature fabrication of highly crystalline SnO$_2$ nanorods. *Adv. Mater.* **2003**, *15*, 1022–1025. [CrossRef]
27. Xu, J.; Li, Y.; Huang, H.; Zhu, Y.; Wang, Z.; Xie, Z.; Wang, X.; Chen, D.; Shen, G. Synthesis, characterizations and improved gas-sensing performance of SnO$_2$ nanospike arrays. *J. Mater. Chem.* **2011**, *21*, 19086–19092. [CrossRef]

28.   Zhang, J.; Guo, J.; Xu, H.; Cao, B. Reactive-template fabrication of porous SnO$_2$ nanotubes and their remarkable gas-sensing performance. *ACS Appl. Mater. Interfaces* **2013**, *5*, 7893–7898. [CrossRef] [PubMed]

29.   Yang, R.; Zhao, W.; Zheng, J.; Zhang, X.; Li, X. One-step synthesis of carbon-coated tin dioxide nanoparticles for high lithium storage. *J. Phys. Chem. C* **2010**, *114*, 20272–20276. [CrossRef]

30.   Tomer, V.K.; Duhan, S. In-situ synthesis of SnO$_2$/SBA-15 hybrid nanocomposite as highly efficient humidity sensor. *Sens. Actuators B Chem.* **2015**, *212*, 517–525. [CrossRef]

31.   Ma, J.; Lei, D.; Duan, X.; Li, Q.; Wang, T.; Cao, A.; Mao, Y.; Zheng, W. Designable fabrication of flower-like SnS$_2$ aggregates with excellent performance in lithium-ion batteries. *RSC Adv.* **2012**, *2*, 3615–3617. [CrossRef]

32.   Gu, D.; Li, X.; Zhao, Y.; Wang, J. Enhanced NO$_2$ sensing of SnO$_2$/SnS$_2$ heterojunction based sensor. *Sens. Actuators B Chem.* **2017**, *244*, 67–76. [CrossRef]

33.   Wan, W.; Li, Y.; Ren, X.; Zhao, Y.; Gao, F.; Zhao, H. 2D SnO2 nanosheets: Synthesis, characterization, structures, and excellent sensing performance to ethylene glycol. *Nanomaterials* **2018**, *8*, 112. [CrossRef] [PubMed]

34.   Aly, K.; Abousehly, A.; Othman, A. Photoelectrical properties of (Sb$_{15}$As$_{30}$Se55)$_{100-x}$Te$_x$ ($0 \leq x \leq 12.5$ at.%) thin films. *J. Non-Cryst. Solids* **2008**, *354*, 909–915. [CrossRef]

35.   Heiland, G.; Kohl, D.; Seiyama, T. (Eds.) *Chemical Sensor Technology*, 1st ed.; Kodansha: Tokyo, Japan, 1988; Volume 1, p. 15.

36.   Xu, H.Y.; Chen, Z.R.; Liu, C.Y.; Ye, Q.; Yang, X.P.; Wang, J.Q.; Cao, B.Q. Preparation of {200} crystal faced SnO$_2$ nanorods with extremely high gas sensitivity at lower temperature. *Rare Met.* **2021**, *40*, 2004–2016. [CrossRef]

37.   Li, T.; Li, L.; Sun, H.; Xu, Y.; Wang, X.W.; Luo, H.; Liu, Z.; Zhang, T. Porous ionic membrane based flexible humidity sensor and its multifunctional applications. *Adv. Sci.* **2017**, *4*, 1600404. [CrossRef] [PubMed]